Precisely Engineered Nitrogen-Doped Hierarchical Porous Carbon from Lignin for High-Rate and Ultra-Stable Supercapacitors

Zhebiao Xu , Siyu Song , Zhuangjia Chen , Wenzhuo Wang , Yushen Huang , Fudong Bai , Riyang Shu , Zhipeng Tian , Chao Wang *

Posted Date: 25 March 2026

doi: 10.20944/preprints202603.2040.v1

Keywords: N-doped porous carbon; KOH; lignin; hydrothermal carbonization; supercapacitor

 doi:10.20944/preprints202603.2040.v1

Article

Precisely Engineered Nitrogen-Doped Hierarchical Porous Carbon from Lignin for High-Rate and Ultra-Stable Supercapacitors

Zhebiao Xu, Siyu Song, Zhuangjia Chen, Wenzhuo Wang, Yushen Huang, Fudong Bai, Riyang Shu, Zhipeng Tian and Chao Wang *

Guangdong Provincial Key Laboratory on Functional Soft Condensed Matter, School of Materials and Energy, Guangdong University of Technology, Guangzhou 510006, China

* Correspondence: chaowang@gdut.edu.cn

Highlights

- Synergistic Urea-KOH Co-Activation Strategy Fabricates Hierarchical Porous Carbon with Ultrahigh Surface Area.
- Optimized Nitrogen Configuration Synergistically Enhances Pseudocapacitance and Interface Kinetics.
- Robust Electrode Material Demonstrates Outstanding Rate Capability and Exceptional Long-Term Cycling Stability.

Abstract

The development of high-performance and sustainable carbon electrodes is increasingly important for next-generation supercapacitors, yet controlling heteroatom doping and hierarchical pore evolution in biomass-derived carbons remains a key challenge. Lignin, as an abundant aromatic biopolymer, offers a structurally rich platform for designing functional carbons, but its rigid cross-linked architecture limits precise pore regulation and efficient nitrogen incorporation. In this work, nitrogen-doped hierarchical porous carbons were engineered from enzymatically treated lignin through a synergistic urea-assisted nitrogen doping and KOH activation strategy. The urea–KOH co-activation drives the coordinated evolution of micropores and mesopores. This approach yields an optimized carbon material possessing a high BET surface area of 2569 $m^2 .g^{-1}$, an interconnected micro–mesoporous architecture, and a favorable distribution of pyridinic, pyrrolic, and graphitic nitrogen species. The engineered pore hierarchy enhances ion transport kinetics, whereas nitrogen functionalities introduce redox-active sites and improve interfacial wettability. As a result, selected material delivers a high specific capacitance of 221 F g^{-1} at 0.5 A g^{-1}, strong rate capability with 84.4% retention at 20 A g^{-1}, and excellent cycling durability with 90.7% capacitance retention after 50,000 cycles. This study demonstrates a mechanistically informed, scalable pathway for coupling enzymatic structural regulation with chemical activation, offering a sustainable route for transforming lignin into high-value carbon electrodes suitable for advanced supercapacitor applications.

Keywords: N-doped porous carbon; KOH; lignin; hydrothermal carbonization; supercapacitor

1. Introduction

The growing demand for sustainable energy storage systems has accelerated research into next-generation electrochemical capacitors [1]. Supercapacitors have emerged as promising candidates due to their superior power density, rapid charge/discharge capabilities, and exceptional cycling stability, filling the critical gap between conventional batteries and capacitors in the energy storage landscape [2,3]. However, the development of high-performance supercapacitors faces fundamental

 doi:10.20944/preprints202603.2040.v1

challenges in electrode design, particularly the need for materials that simultaneously possess high specific surface area, optimized pore structure, and tailored surface functionality to facilitate both electric double-layer capacitance and pseudocapacitive contributions [4].

Biochar has gained significant attention as a sustainable carbon source for supercapacitor electrodes, offering distinct advantages over conventional fossil fuel-derived carbons. As a renewable carbon material, biochar boasts abundant raw material sources (e.g., crop straws, wood, algae) and prominent benefits including wide distribution, low cost, and environmental friendliness [5]. Unlike fossil fuel-dependent carbons, biochar production enables a negative carbon emission cycle. More importantly, the diversity of biomass precursors with their inherent hierarchical structures (such as natural multi-dimensional pore channels) provides greater flexibility for tailoring carbon material properties [6].

Among various biomass components, lignin stands out as an ideal precursor for advanced carbon materials [7]. Its natural three-dimensional aromatic structure, characterized by rigid benzene rings and cross-linked networks, exhibits higher thermal stability during pyrolysis, effectively inhibiting carbon skeleton densification while facilitating the development of hierarchical pore channels [8,9]. The abundant phenolic hydroxyl and methoxy functional groups on lignin's molecular skeleton serve as efficient grafting sites for heteroatoms, enabling precise in-situ doping - a crucial advantage for enhancing supercapacitor performance [10,11].

The preparation methodology significantly influences the final properties of biochar-based electrodes. Traditional chemical activation methods (e.g., using KOH or H_3PO_4), while effective for surface area enhancement, often pose environmental concerns [12,13]. Recently, enzymatic treatment has emerged as a green pretreatment approach, where selective degradation of biomass components by cellulases can pre-construct hierarchical porous structures [14–16]. This bio-inspired strategy not only increases specific surface area and pore volume during subsequent processing [17] but also enhances electrode-electrolyte compatibility through preserved oxygen functional groups [18,19].

Supercapacitors are primarily categorized into electric double-layer capacitors (EDLCs) and pseudocapacitors based on their energy storage mechanisms [20]. While EDLCs rely on electrostatic adsorption at the electrode-electrolyte interface, pseudocapacitors achieve higher energy density through fast, reversible faradaic reactions. The integration of heteroatoms such as nitrogen into carbon matrices has proven particularly effective for enhancing supercapacitor performance [21,22]. Nitrogen functionalization (e.g., pyridinic-N, pyrrolic-N) introduces pseudocapacitive effects while improving surface wettability and electrical conductivity, significantly boosting both specific capacitance and rate capability [23–25].

Despite these advances, critical challenges remain in developing nitrogen-doped hierarchical porous carbons. The quantitative understanding of capacitance contributions from EDLC and pseudocapacitance mechanisms needs further refinement. The coupling between biological pretreatment and chemical activation, particularly regarding nitrogen doping's influence on pore evolution and surface properties, requires deeper investigation. Furthermore, establishing precise structure-property relationships between microscopic characteristics (pore architecture, nitrogen configuration) and macroscopic performance metrics remains challenging but essential for rational material design.

To address the aforementioned issues, this study proposes a strategy employing urea-KOH co-activation synergized with enzymatic pretreatment of lignin, aiming to construct a nitrogen-doped hierarchical porous carbon material. By systematically regulating the enzymatic hydrolysis conditions and activation parameters, we seek to elucidate the regulatory mechanisms of nitrogen doping on the pore structure, surface functional groups, and capacitive behavior. A key focus will be the precise analysis of the synergistic contribution ratio between the electric double-layer and pseudocapacitance, aiming to provide new insights for designing high-performance supercapacitor electrode materials.

 doi:10.20944/preprints202603.2040.v1

2. Experimental

2.1. Preparation of Activated Carbon

Enzymatic hydrolysis lignin (EHL) was sourced from Sinopec (Dalian) Petrochemical Research Institute. All reagents used, including potassium hydroxide (KOH, 85%) from Tianjin Zhiyuan Chemical Reagent Co., Ltd., urea was purchased from Tianjin Damao Reagent Factory ($CO(NH_2)_2$, 99%), hydrochloric acid (HCl, 37%) and sulfuric acid (H_2SO_4, 98%) from Guangdong Guangshi Reagent Technology Co., Ltd., were of analytical grade and required no further purification.

The physicochemical properties of the enzymatic hydrolysis lignin (EHL) precursor are summarized in Tables 1 and 2. The proximate analysis shows that the raw EHL contains a moisture content of 6.00 wt%, volatile matter of 60.06 wt%, fixed carbon of 31.05 wt%, and an ash content of 2.89 wt%. The ash content, which directly reflects the inorganic impurity level, indicates a relatively low mineral constituent in the lignin material. Furthermore, the ultimate analysis (elemental composition) demonstrates that the EHL is primarily composed of carbon (58.6 wt%), oxygen (32.88 wt%), hydrogen (3.75 wt%), and nitrogen (0.59 wt%), with sulfur being undetected. The low sulfur and ash content confirm the high organic purity of the lignin precursor, making it suitable for the synthesis of high-quality porous carbon materials. Prior to use, the EHL was thoroughly washed with deionized water and dried to minimize residual soluble impurities.

Table 1. EHL Organic elemental analysis test results.

	Sample	N (%)	C (%)	H (%)	S (%)	O (%)
CHNS mode	EHL	0.605	58.849	3.755	0	32.953
O mode	EHL	0.576	58.414	3.752	0	32.801

Table 2. EHL Coal industry analysis test results.

Sample	Moisture M_{ad} (%)	Ash A (%)		Volatile matter V (%)			Fixed carbon FC_{ad} (%)
		A_{ad}	A_d	V_{ad}	V_d	V_{daf}	
EHL	6.00	2.89	3.07	60.06	63.89	65.91	31.05

Firstly, 10 g EHL was washed thoroughly with deionized water and dried overnight. Enzymatically hydrolyzed lignin samples were precisely proportioned with urea at mass ratios of 1:1, 1:2, 1:3, and 1:4, followed by homogeneous dispersion in 120 mL of deionized water. Subsequently, 1.84 mL of concentrated sulfuric acid (98 wt.%) was introduced into the mixture under continuous magnetic stirring to ensure thorough dissolution and reactant homogeneity. The mixture was stirred for 30 minutes and sonicated for 15 minutes to enhance dispersion. The pretreated solution was then transferred to a 250 ml PTFE-lined stainless steel autoclave and subjected to hydrothermal treatment at 200 ℃ for 24 hours, afterwards it was naturally cooled to room temperature. The resulting hydrothermal carbon of nitrogen-doped (HCN) product was filtered, washed to neutral with deionized water, and dried at 70℃ overnight. The resulting hydrothermal carbons were labeled HCN-1 through HCN-4, corresponding to the increasing urea-to-EHL ratios.

For activation, a 1 M KOH solution was prepared by dissolving 6.59 g of 85% KOH in deionized water, then diluting to a final volume of 100 ml. The dried HCN-1 through HCN-4 was then impregnated with KOH at mass ratios of 1:3. The selection of these alkali ratios was determined by the consumption of KOH to HCN during chemical activation. The KOH-HCN mixtures were heated in a muffle furnace under an argon atmosphere (100 ml/min) for 30 minutes, then further heated to 800℃ at a rate of 3℃/min and held for 1 hour to complete activation. After cooling, the samples were thoroughly rinsed with 10 vol% HCl to remove any residual inorganic impurities, followed by deionized water washing until neutral, and dried at 70℃ overnight. The resulting porous activated carbons were denoted as HPCN-1 toHPCN-4.

 doi:10.20944/preprints202603.2040.v1

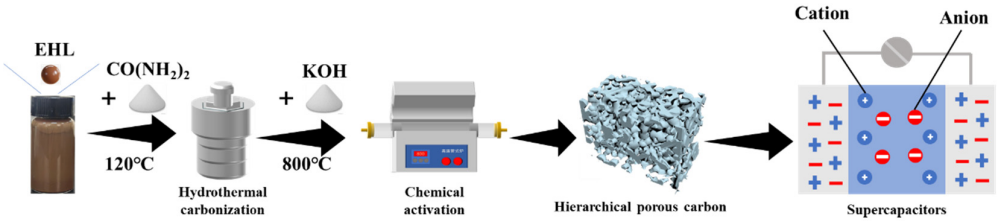

Figure 1. Schematic diagram of the preparation process of nitrogen-doped hierarchical porous carbon.

2.2. Materials Characterizations

The specific surface area and pore characteristics were determined by nitrogen adsorption-desorption isotherms using a Micromeritics ASAP 2460 surface analyzer. The morphological features of the samples were examined by scanning electron microscopy (SEM) using the TESCAN MIRA LMS, providing high-resolution imaging of structural features. Fourier transform infrared spectroscopy (FTIR, Thermo Fisher Scientific Nicolet iN10) was employed to identify functional groups present in the samples before and after hydrothermal treatment, offering insights into chemical modifications and their impact on material properties. Elemental composition and bonding states were analyzed by X-ray photoelectron spectroscopy (XPS, Thermo Fischer ESCALAB 250Xi), providing detailed insight into surface chemistry and functional groups. Crystallographic properties were investigated via X-ray diffraction (XRD, Ultima IV) over a 5° to 90° scanning range, elucidating the degree of structural order. Raman spectroscopy (Lab Ram HR Evolution) was conducted at room temperature with a 532 nm excitation wavelength to assess the graphitic and amorphous carbon content within the samples.

To gain deeper insights into the role of heteroatoms, we performed density functional theory (DFT) simulations to investigate the impact of nitrogen doping on the adsorption energy, density of states (DOS), and band structure. The calculations were conducted using the Vienna Ab initio Simulation Package (VASP) with the Perdew-Burke-Ernzerhof (PBE) functional under the generalized gradient approximation (GGA). Projector augmented wave (PAW) potentials were employed with a plane-wave cutoff energy of 520 eV, and van der Waals interactions were incorporated via the DFT-D3 empirical correction. Geometry optimization criteria were set at a force convergence below 0.02 eV/Å and an energy convergence of 1×10^{-5} eV. Monkhorst-Pack k-point meshes of 2×2×1 and 4×4×1 were used for optimization and DOS calculations, respectively.

2.3. Electrochemical Measurements

The working electrode was prepared by mixing the active material, conductive agent (acetylene black), and binder (polytetrafluoroethylene, PTFE) in a mass ratio of 8:1:1. This mixture was homogenized in ethanol to form a uniform slurry, which was then coated onto a nickel foam current collector (1×1 cm^2). The coated electrode was dried at 80 °C for 12 hours under vacuum to remove the solvent, followed by pressing at 10 MPa to ensure good adhesion and electrical contact. The typical active material loading was approximately 2.0 mg/cm^2.

The electrochemical performance was investigated by an electrochemical workstation (CHI 760E, Chenhua, Shanghai), which used a conventional three-electrode setup with a 6 M KOH solution as the electrolyte. The reference electrode was Hg/HgO and the counter electrode was Pt. Cyclic voltammetry (CV) measurements were carried out at different scan rates with a voltage window of -1.0 to 0 V. Electrochemical impedance spectroscopy (EIS) was performed at a scan rate of 1 mV/s with a frequency range of 10-2 to 105 Hz. Galvanostatic charge–discharge (GCD) was performed at different current densities. The specific capacitance can be calculated by using the GCD curve through Equation.

 doi:10.20944/preprints202603.2040.v1

$$C_m = I \triangle t/(\mathrm{m} \triangle \mathrm{V}) \quad (1)$$

where I denotes discharge current (A),△t denotes discharge time (s), m denotes quality of electrode material (g),△V denotes voltage window (V) and C_m denotes specific capacitance (F/g).

The energy density E (Wh/kg) and power density P (W/kg) based on GCD curves is given by Equations (2) and (3) [26].

$$E = \frac{C_m}{2} \times \triangle V^2 \times 1/3.6 \quad (2)$$

$$P = \frac{E}{\triangle t} \times 3600 \quad (3)$$

3. Results and Discussion

3.1. Morphology and Structure Properties of Hierarchical Porous Carbon

As shown in Figure 2a, all HPCN samples displayed a combination of type-I and type-IV isotherms, indicating the coexistence of micropores and mesopores. The nitrogen-doped porous carbon exhibits a Type I/IV composite isotherm with a pronounced adsorption plateau at p/p^0 = 0.8-1.0, indicating a well-developed micro-mesoporous network that synergistically enhances electrolyte accessibility and charge storage mechanisms [27]. As shown in Table 1, specific surface area (S_{BET}) of HPCN-2 reaches 2569.45 m^2/g, with the micropore area (S_{micro}) attains 2117.98 m^2/g, both being the highest values among the series, indicating a high density of microporous walls and a prominent reservoir effect that provides abundant active sites. Meanwhile, the mesopore volume (V_{meso}) of 0.2893 cm^3/g and mesopore volume fraction (W_{meso}) of 23.98% show outstanding performance in mesoporous structural parameters, significantly surpassing the underdeveloped mesoporosity in HPCN-1 and HPCN-3 as well as the slightly lower mesopore volume in HPCN-4. Notably, the mesopore area fraction (C_{meso}) of HPCN-2 peaks at 17.52%, and when combined with a moderate average pore size of 1.8734 nm, synergistically enabling a hierarchical pore architecture where micropores dominate active-site adsorption while mesopores facilitate accelerated ion diffusion. This structure not only ensures efficient adsorption of small molecules but also optimizes the transport pathways for large molecules. As shown in Figure 2b,c, the narrow pore size distribution—achieved through optimized nitrogen doping at a 1:2 lignin-to-urea ratio—indirectly reflects the structural directing role of nitrogen species in creating uniform pore channels that subsequently facilitate uniform K^+ insertion/extraction kinetics [28]. This structural synergy translates to exceptional electrochemical performance, attributed to the hierarchical porosity and nitrogen-rich surface functionalities that synergize double-layer capacitance and pseudocapacitive contributions [29]. These findings underscore the pivotal role of stoichiometric nitrogen doping and pore engineering in advancing carbon-based supercapacitors, establishing HPCN-2 as a benchmark electrode material for high-performance energy storage systems.

Table 3. Summary of the structure parameters for the prepared HPCN samples.

HPCN Samples	S_{BET} (m^2/g)	S_{micro} (m^2/g)	S_{meso} (m^2/g)	C_{meso} (%)	V_{total} (cm^3/g)	V_{micro} (cm^3/g)	V_{meso} (cm^3/g)	W_{meso} (%)	d_{pore} (nm)
HPCN-1	1823.87	1577.13	245.91	**13.48**	0.8183	0.6502	0.1561	**19.08**	1.7939
HPCN-2	2569.45	2117.98	450.18	**17.52**	1.2062	0.8921	0.2893	**23.98**	1.8734
HPCN-3	1990.89	1750.01	238.93	**12.00**	0.9690	0.7066	0.2237	**23.06**	1.9538
HPCN-4	2294.64	1926.01	367.68	**16.02**	1.0456	0.7958	0.2374	**22.70**	1.8218

 doi:10.20944/preprints202603.2040.v1

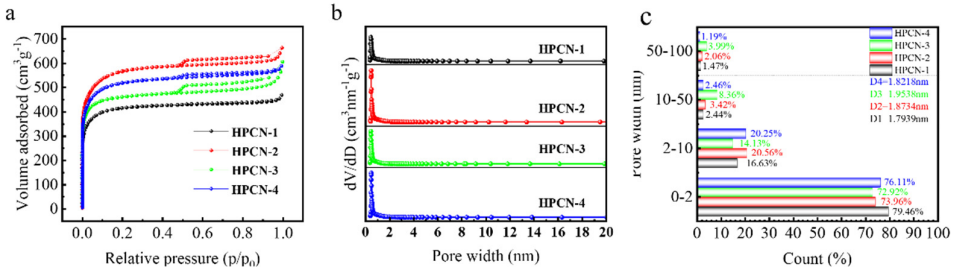

Figure 2. (a)N_2 adsorption-desorption isotherms of HPCN-1~HPCN-4, (b)pore size distributions (PSD) curves, (c)PSD of HPCN-1~HPCN-4.

From microstructural and elemental analyses, enzymatic lignin (Figure 3a) exhibits a dense lamellar structure with limited porosity characteristic of natural lignin's cross-linked polymer architecture. Hydrothermal treatment with urea at varying ratios induces structural divergence in the HCN series (Figure 3b-e), low urea ratios (e.g., HCN-1) produce sporadic particulate deposits with underdeveloped micropores, while excessive urea (HCN-4) causes rigidified structures with dispersed pores [30]. KOH activation of HPCN-2 generates a hierarchical porous architecture comprising interconnected macropores (>50 nm) for electrolyte accessibility, mesopores (2-50 nm) facilitating ion diffusion, and micropores (<2 nm) enhancing surface interactions [31,32]. This configuration achieves a BET-specific surface area of 2569.45 m^2/g, with mesopores constituting a dominant fraction critical for rapid charge transfer. Nitrogen doping (pyridinic/pyrrolic N) (confirmed by EDS mapping in Figure 3j-l) covalently integrates functional sites into the carbon matrix, creating synergistic interfaces that amplify pseudocapacitive contributions while maintaining conductivity. The hierarchical porosity of HPCN-2 demonstrates enhanced electrolyte wettability and ion accessibility. The synergistic interplay between nitrogen-functionalized micropores and continuous mesopores enables efficient charge storage through both double-layer capacitance and pseudocapacitive mechanisms [33].

Fourier transform infrared (FTIR) spectroscopy (Figure 4a) elucidates structural evolution during carbonization and activation. EHL exhibits characteristic absorption bands in the O-H stretching (3400 cm^{-1} region), aromatic C=C stretching (1600–1450 cm^{-1}), and C-O stretching (1260 cm^{-1}) regions [34], which correlate with its dense aromatic framework and abundant polar functional groups. These structural features align with the limited porosity observed in the smooth surface morphology imaged via SEM(Figure 3a). During hydrothermal carbonization (HCN-2), the attenuation of O-H and C-O absorption bands, coupled with the emergence of a carbonyl-related peak (~1700 cm^{-1}), indicates urea-mediated structural deconstruction. This transformation involves ether bond cleavage and demethoxylation, disrupting the rigid lignin matrix and enhancing molecular mobility, thereby facilitating limited pore development. Subsequent KOH activation to produce porous activated carbon (HPCN-2) enhances polar functional groups (e.g., carboxyl, pyridinic N), which synergistically drive directional pore expansion through chemical etching of aromatic layers guided by nitrogen-doped defects and template-assisted mechanisms where urea-derived nitrogen species constrain carbon condensation [35]. This dual process generates hierarchical porosity, optimizing surface area and charge transfer kinetics.

Raman spectroscopy investigations of the HPCN series porous carbons (Figure 4b) reveal that varying urea-to-enzymatic lignin mass ratios (1:1 to 1:4) significantly influence the structural order of the carbon frameworks. As illustrated in the Raman spectra, the intensity ratio of the D-band (1330 cm^{-1}, associated with disordered structures or defect states) to the G-band (1585 cm^{-1}, corresponding to sp^2-hybridized graphitic carbon planes) exhibits a systematic trend. With increasing urea doping ratios from 1:1 to 1:4, the I_D/I_G value decreases from 0.98 (HPCN-1) to a minimum of 0.96 (HPCN-2), followed by a gradual rise to 1.02 (HPCN-4). Notably, HPCN-2 demonstrates the lowest I_D/I_G value (0.96), indicating superior graphitization and minimal structural defects, which synergistically aligns with nitrogen doping site distribution observed in XPS analysis (Figure 5d). In supercapacitor

 doi:10.20944/preprints202603.2040.v1

electrode applications, the crystalline structure of HPCN-2 offers dual functional advantages. First, its highly graphitized microstructure shortens π - π conjugation pathways, significantly enhancing intrinsic electrical conductivity and optimizing rate performance by enabling efficient charge transport under high-current conditions [36]. Second, the reduced defect density minimizes disordered active site aggregation, thereby stabilizing the ion adsorption/desorption interfaces and mitigating structural collapse during cyclic operations [37]. This structural integrity, combined with nitrogen doping effects (evidenced by XPS-verified functional groups), creates a synergistic platform where ordered carbon frameworks host optimized active sites. The graphitic matrix could enhance pseudocapacitive contributions through electron delocalization, while nitrogen species might modulate surface wettability and interfacial charge transfer kinetics.

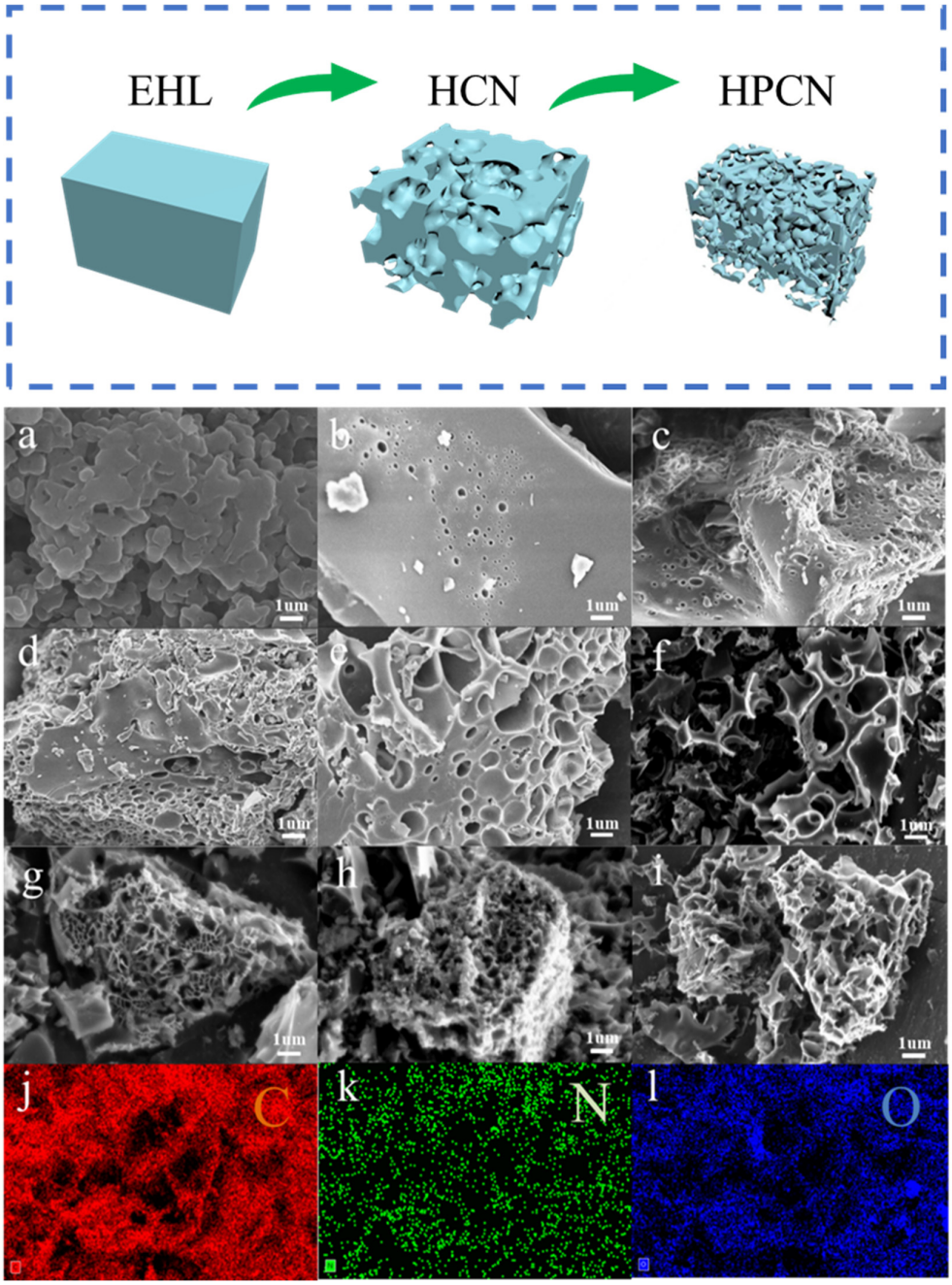

Figure 3. SEM images of EHL(a), HCN-1~HCN-4(b-e), and HPCN-1~HPCN-4(f-i), the corresponding EDX elemental mapping images of HPCN-2(j-l).

 doi:10.20944/preprints202603.2040.v1

To visually complement the spectroscopic and structural analyses presented, Figure 4c schematically illustrates the urea decomposition pathways and nitrogen incorporation process during hydrothermal treatment. The diagram explicitly depicts how urea decomposes into NH_3 and isocyanic acid under acidic hydrothermal conditions, with these reactive intermediates subsequently attacking the oxygen-containing functional groups—particularly phenolic hydroxyl (C–OH) and methoxy groups—on the lignin skeleton. This step initiates the preliminary nitrogen doping and structural loosening of the rigid lignin matrix, consistent with the FTIR-observed attenuation of O-H and C-O bands. Furthermore, the illustration delineates the progressive transformation from the initial dense lignin architecture into a nitrogen-enriched porous carbon framework, highlighting the formation of a heterogeneous nitrogen doping network comprising pyridinic N, pyrrolic N, and graphitic N species. Such visual elaboration reinforces the mechanism by which urea-derived nitrogen precursors, in synergy with KOH activation, facilitate the development of hierarchical porosity and optimized nitrogen functionality, as corroborated by the Raman and XPS results.

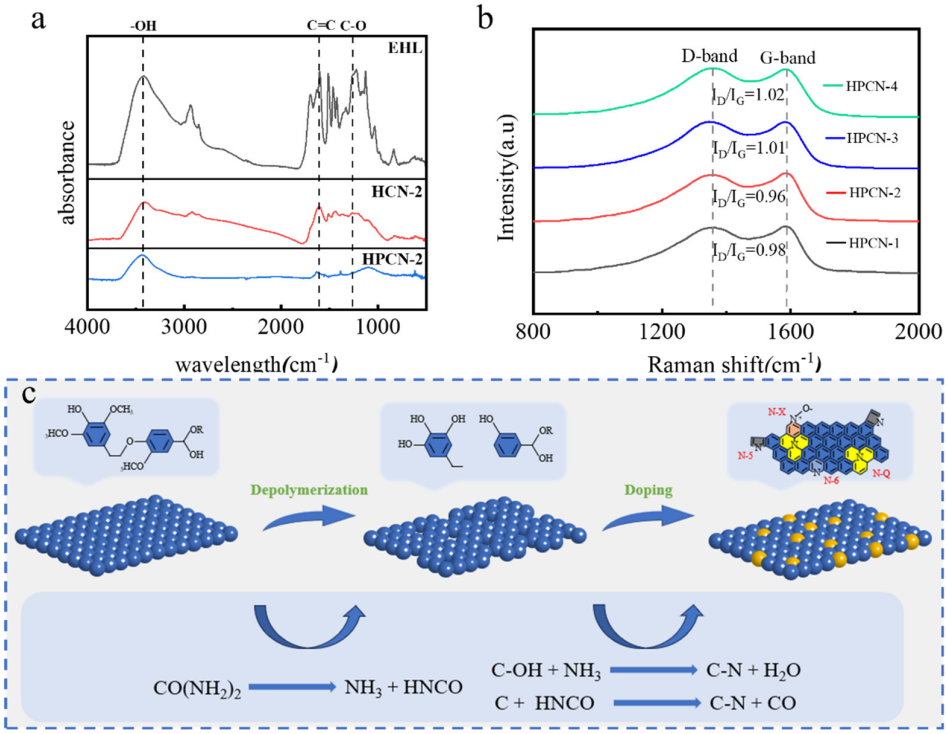

Figure 4. (a)Fourier transform infrared spectroscopy of EHL, HCN-2 and HPCN-2, (b) raman spectra of HPCN-1~HPCN-4, (c) synthesis strategy for nitrogen-doped porous carbon.

As shown in Figure 5a, the intensity of nitrogen characteristic peaks in the samples first rises and then falls with increasing urea loading (mass ratio of enzyme-treated lignin to urea from 1:1 to 1:4). Among which, the N 1s peak intensity of HPCN-2 is remarkably higher than that of other samples, indicating a peak nitrogen doping level that directly correlates with the amount of urea introduced as the nitrogen source. Further deconvolution of the N 1s high-resolution spectrum (Figure 5d) reveals that HPCN-2 features a polymorphous coordination configuration of nitrogen species, including pyridinic nitrogen (N-6, 398.6 eV), pyrrolic nitrogen (N-5, 399.8 eV), graphitic nitrogen (N-Q, 400.9 eV), and oxidized nitrogen (N-X, 402.2 eV), with balanced peak area contributions that form a complex nitrogen-doped network [38]. Compared to HPCN-1, which suffers from insufficient nitrogen doping due to inadequate urea supply, HPCN-3 and HPCN-4 potentially experience nitrogen species agglomeration or carbon structure disruption because of excessive urea. In contrast, this distinctive nitrogen distribution in HPCN-2 demonstrates

 doi:10.20944/preprints202603.2040.v1

pronounced advantages in charge storage mechanisms. Specifically, high contents of pyridinic and pyrrolic nitrogen endow additional pseudocapacitance through surface redox reactions. Meanwhile, oxidized nitrogen and graphitic nitrogen optimize interfacial wettability and electrolyte ion adsorption. Together, these effects establish critical synergistic enhancements. In supercapacitor electrode applications, nitrogen species could not only enhance specific capacitance through surface redox reactions but also modulate surface charge distribution to improve electrolyte wettability and reduce ionic transport resistance, thereby maintaining outstanding cyclic stability and energy density under high-rate charge-discharge conditions [39].

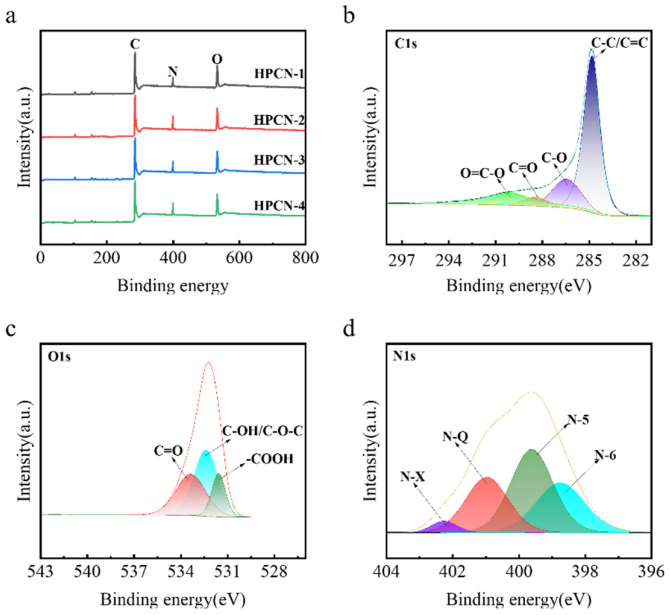

Figure 5. (a) XPS survey spectra of HPCN-1, HPCN-2, HPCN-3, HPCN-4, (b-d) High-resolution XPS spectrum of C 1s, O 1s, and N 1s of HPCN-2.

3.2. Electrochemicaltests

From the perspective of specific capacitance performance, Figure 6c shows that at a current density of 0.5 A/g, the GCD curve of HPCN-2 displays the longest charge-discharge duration, corresponding to a specific capacitance value of 221 F/g, which is significantly higher than those of HPCN-1, HPCN-3, and HPCN-4 under the same system, reflecting its excellent synergistic energy storage capability of electric double-layer capacitance (EDLC) and pseudocapacitance. From the CV curves in Figure 6a, HPCN-2 demonstrates the largest integrated area at a scan rate of 5 mV/s, with high-intensity and well-symmetric redox peaks, intuitively reflecting its efficient faradaic reaction kinetic process, which lays an electrochemical foundation for its high specific capacitance [40,41]. The double-layer capacitance (Cdl) of the catalysts was measured and analyzed to evaluate their intrinsic activity and rate capability as electrode materials for supercapacitors. As illustrated in Figure 6b, HPCN-2 exhibits the highest Cdl value (0.413 mF/cm^2), indicating it possesses the largest electrochemically active surface area (ECSA), which provides a fundamental basis for achieving high specific capacitance. Furthermore, the excellent linear relationship between the current response and scan rate reveals a highly reversible electric double-layer charge storage mechanism, directly suggesting outstanding rate capability and high power density during rapid charge/discharge processes. Consequently, HPCN-2 is confirmed as the most promising electrode candidate.

In terms of rate capability, Figure 6d,e reveal the exceptional adaptability of HPCN-2. When the scan rate increases from 5 mV/s to 100 mV/s (Figure 6d), its CV curves consistently maintain clear redox peaks, and the peak current increases linearly with the scan rate, indicating the material's rapid

 doi:10.20944/preprints202603.2040.v1

electron transport capability at surface active sites. In GCD tests under different current densities (Figure 6e), even when the current density increases to 20 A/g, the charge-discharge curves still retain an approximately near-triangular symmetric shape, with a significant advantage in charge-discharge time proportion, reflecting low internal resistance and rapid ion diffusion characteristics. By comparing the specific capacitance retention rates within the current density range of 1-20 A/g in Figure 6f, the C value of HPCN-2 only slightly decreases from approximately 221 F/g to 180 F/g, with a much smaller decline compared to other samples (e.g., the C value of HPCN-1 drops below 120 F/g at 20 A/g), proving its stable energy storage capability under high-power density scenarios with no significant capacity fading, which is closely related to the material's excellent pore structure and conductive network construction.

To further elucidate the remarkable energy storage performance of the HPCN-2 electrode material, we investigated the relationship between its fast kinetics (EDLC) and low kinetics contributions (PC), the relationship between the thus confirmed and pseudo capacitance of electric double layer capacitance coexist. The corresponding capacitive contributions can be determined using the formula below [26].

$$i = kv^b \tag{4}$$

$$log(i) = blog(v) + \log(k) \tag{5}$$

where i and v denote the current density and the scanning rate respectively. The value of b indicates the slope in Eq.

The influences of diffusion control and surface control in the electrochemical process can be assessed through the value of b. Values of b nearing 0.5 suggest that the diffusion process primarily influences the capacitive contribution. In contrast, when b approaches 1, it signifies that the capacitive contribution corresponds to a surface-controlled response. As shown in Figure 6g, a linear relationship exists between log(v) and log(i). During the charging process, a calculated b value of 0.99134 suggests that HPCN-2 demonstrates characteristics of ideal electric double-layer capacitance. Additionally, we employed the Dunn method to quantitatively differentiate between the contributions controlled by capacitance($k_1v^{1/2}$) and those governed by diffusion (k_2), as shown in the following equations.

$$i = k_1v + k_2v^{1/2} \tag{6}$$

$$i/v^{1/2} = k_1v^{1/2} + k_2 \tag{7}$$

Figure 6i demonstrates that the contribution controlled by capacitance of HPCN-2 at a scanning rate of 100 mV s^{-1} amounts to 98.46%. This indicates that the fast reaction kinetics primarily dictate the electrochemical behavior of this electrode. With the increase of the scanning rate, the contribution of capacitive control of HPCN-2 gradually rises from 93.47% to 98.46% (Figure 6h), while the diffusion-controlled contribution decreases from 6.53% to 1.54%. This observation confirms that the electrochemical performance of HPCN-2 is predominantly capacitive-controlled and exhibits ideal capacitive characteristics.

The superior electrochemical performance of HPCN-2, as demonstrated by its high specific capacitance (221 F/g at 0.5 A/g) and outstanding rate capability (84.4% retention at 20 A/g), can be directly attributed to its optimized surface chemistry, specifically the nitrogen doping configuration. As quantitatively analyzed from the XPS N 1s spectra, HPCN-2 possesses not only the highest total nitrogen content (3.84 at%) among the series but also the most favorable distribution of nitrogen species. It exhibits the highest relative proportion of redox-active pyridinic-N (35.2%), which contributes significantly to the pseudocapacitance observed in the CV curves (Figure 6a). Concurrently, its substantial graphitic-N content (24.1%) enhances the electrical conductivity of the carbon framework, facilitating rapid charge transfer and underpinning the excellent rate performance. In contrast, the inferior capacitance and rate capability of HPCN-1, HPCN-3, and HPCN-4 correlate well with their suboptimal nitrogen content and/or configuration. This empirical

 doi:10.20944/preprints202603.2040.v1

correlation firmly establishes that the synergistic effect of a high specific surface area, a hierarchical pore structure, and an optimized nitrogen configuration is the key to achieving high-performance in lignin-derived porous carbon electrodes.

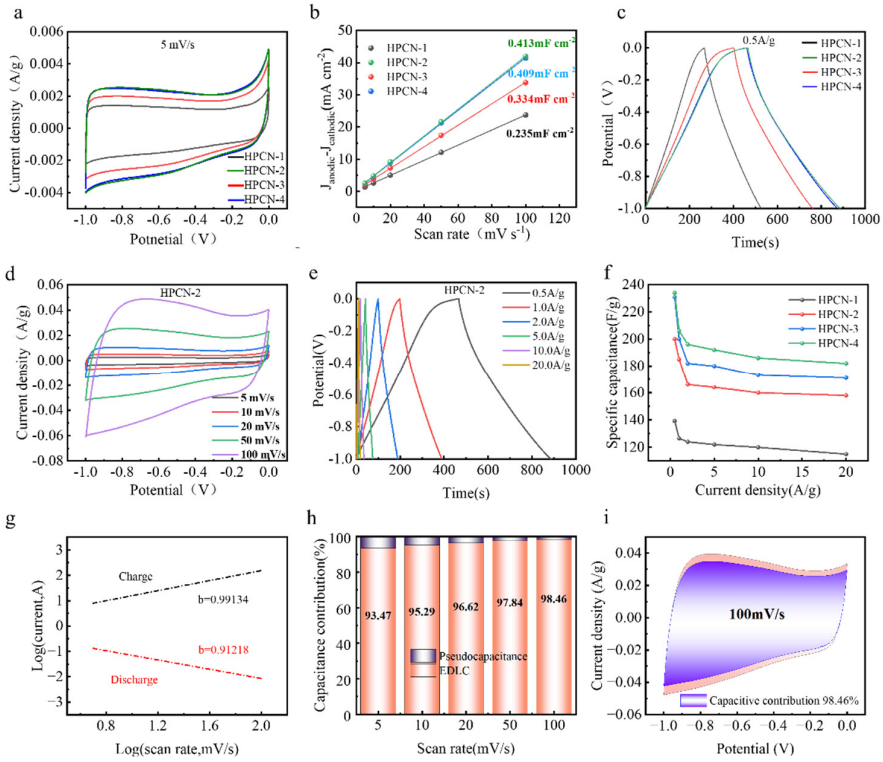

Figure 6. (a) CV curves of HPCN-1, HPCN-2, HPCN-3 and HPCN-4 at 5mV/s, (b) Cdl, (c) GCD curves of HPCN-1, HPCN-2, HPCN-3 and HPCN-4 at 0.5 A/g, (d) HPCN-2 electrode at 5–100mV/s, (e) HPCN-2 electrode at 0.5–20 A/g, (f) C values of the four electrodes with current density from 0.5 to 20 A/g, (g) Corresponding log (i) vs log (v) curves at specific peak currents, (h) Histogram showing the capacitive contribution at different current densities for HPCN-2, and (i) Capacitive contribution at a scan rate of 100 mV/s.

Table 4. XPS-derived nitrogen species distribution and corresponding electrochemical performance.

Sample	Total N (at%)	N-6 (%)	N-5 (%)	N-Q (%)	Capacitance (F/g)	Retention (%)
HPCN-1	2.91	31.5	26.3	22.1	129	76.2
HPCN-2	3.84	35.2	28.7	24.1	221	84.4
HPCN-3	3.25	29.8	30.2	25.4	188	79.1
HPCN-4	3.57	27.6	31.9	26.8	218	81.3

The results demonstrate that nitrogen doping significantly modulates the adsorption behavior of lithium. The adsorption energies (ΔE) were calculated relative to Li in the bcc bulk structure (-3.80 eV). For the pristine carbon layer, the Li adsorption energy was 0.43 eV, indicating relatively weak adsorption. In contrast, pyridinic-N and pyrrolic-N configurations showed much stronger adsorption, with ΔE values of -2.74 eV and -2.53 eV, respectively, while graphitic-N exhibited a ΔE of 0.52 eV, even weaker than the undoped system. This trend highlights that although nitrogen itself may weaken adsorption, the defect structures induced by pyridinic-N and pyrrolic-N enhance adsorption significantly.

Furthermore, density of states analysis revealed that nitrogen doping introduces new peaks near the Fermi level, altering the electronic structure substantially compared to the pure carbon layer. These changes suggest enhanced electronic interaction at the adsorption sites, which aligns with the

 doi:10.20944/preprints202603.2040.v1

observed adsorption energy trends. In summary, the DFT simulations confirm that heteroatom doping—particularly in the form of pyridinic-N and pyrrolic-N—plays a critical role in strengthening Li adsorption and modifying electronic properties, underscoring its importance in the design of advanced adsorption materials.

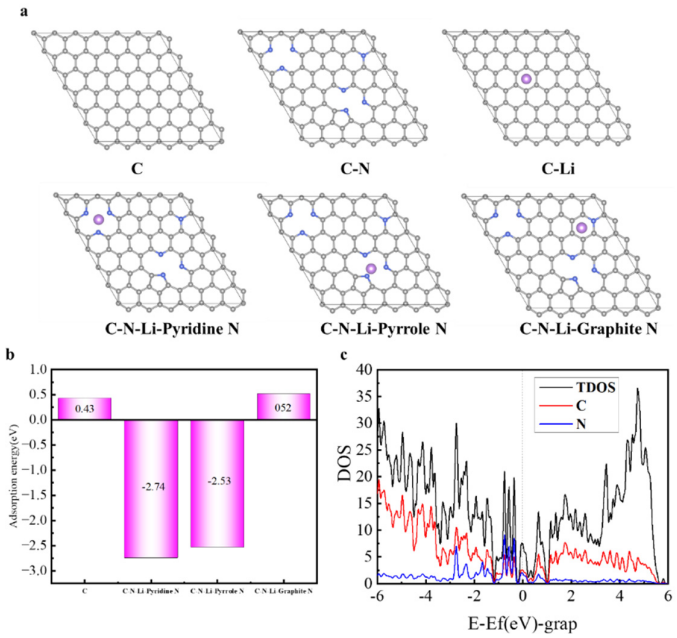

Figure 7. (a) The theoretical calculation models basing on defective graphene model, (b) The adsorption energy of lithium ion onto the defective graphene models. (c) Adsorption energy of nitrogen doping on defective graphene models.

A critical assessment of the specific capacitance achieved by HPCN-2 (221 F/g at 0.5 A/g) within the context of recent literature on lignin-derived carbons (as summarized in Table 5) reveals its distinct advantages when key experimental variables are considered. While materials like Fe-NLC report a higher capacitance of 264 F/g [45], its synthesis involves transition metal incorporation, adding complexity and cost. In contrast, HPCN-2 is derived via a sustainable, metal-free, urea-KOH co-activation strategy. Similarly, compared to LPRAC-20% (217.3 F/g) [44] and LPC-150 (214.03 F/g) [46], which were also tested at 0.5 A/g in 6M KOH, HPCN-2 demonstrates a clear performance edge. This advantage is further amplified by its exceptional rate capability (84.4% retention at 20 A/g), a metric often not highlighted in comparative studies. Furthermore, unlike materials tested under more favorable, lower current densities (e.g., ACNFs at 0.1 A/g [42]), the performance of HPCN-2 was validated under more demanding conditions, underscoring its robust charge storage kinetics. Therefore, HPCN-2 not only delivers competitive specific capacitance but does so through a green synthesis route while excelling in high-rate performance and long-term stability, establishing it as a uniquely balanced and promising candidate for advanced supercapacitor electrodes.

Table 5. Comparison of the specific capacitance of the electrode materials in this paper with those reported in other literatures.

Sample	Electrolytes	Test condition	Specific capacitance	References
KL-8	6M KOH	0.25A/g	88F/g	[6]
ACNFs	1M H_2SO_4	0.1 A/g	182 F/g	[42]
LMSC-L1	6M KOH	1A/g	200F/g	[43]
LPRAC-20%	6M KOH	0.5A/g	217.3F/g	[44]

 doi:10.20944/preprints202603.2040.v1

Fe-NLC	6M KOH	0.5A/g	264 F/g	[45]
LPC-150	6M KOH	0.5A/g	214.03 F/g	[46]
HPCN-2	6M KOH	0.5A/g	221F/g	This work

Electrochemical characterization reveals exceptional charge storage capability and cycling stability in symmetric two-electrode configurations. At current densities ranging from 0.5 to 10 A/g, the specific capacitance declines only marginally from 208.05 F/g to 172.56 F/g, achieving a capacitance retention of 82.94%, which underscores its outstanding rate capability for high-power applications. This performance stems from the synergistic interplay between KOH-activated pore structures and urea-derived nitrogen doping sites, which collectively enhance ion diffusion kinetics and surface charge adsorption [47,48]. Furthermore, cyclic stability testing under a 5 A/g current density reveals a capacitance retention of 90.7% after 50,000 cycles, significantly outperforming most carbon-based electrode materials. This exceptional durability reflects the structural integrity of HPCN-2, where minimized defect density and robust carbon frameworks mitigate active site degradation and pore collapse during prolonged cycling [49]. The near-rectangular CV profiles and symmetric triangular galvanostatic charge-discharge (GCD) curves further validate the reversibility of charge storage mechanisms, characterized by low internal resistance and minimized interfacial charge-transfer barriers [50]. By synergizing high energy density from pseudocapacitive nitrogen functionalities with superior power density enabled by rapid ion transport in hierarchical pores, HPCN-2 emerges as a promising candidate for next-generation supercapacitors. Its dual advantages of structural stability and tunable electrochemical activity position it as a promising candidate for advanced energy storage systems requiring both long operational lifespan and high-rate capability.

This material exhibits a high energy density of 28.89 W h/kg at a power density of 250 W/kg, for a better comparison with the previously reported porous carbon materials. Furthermore, when the power density is increased to 5000 W/kg, it still maintains an energy density of 23.97 W h/kg, which provides excellent energy storage performance.

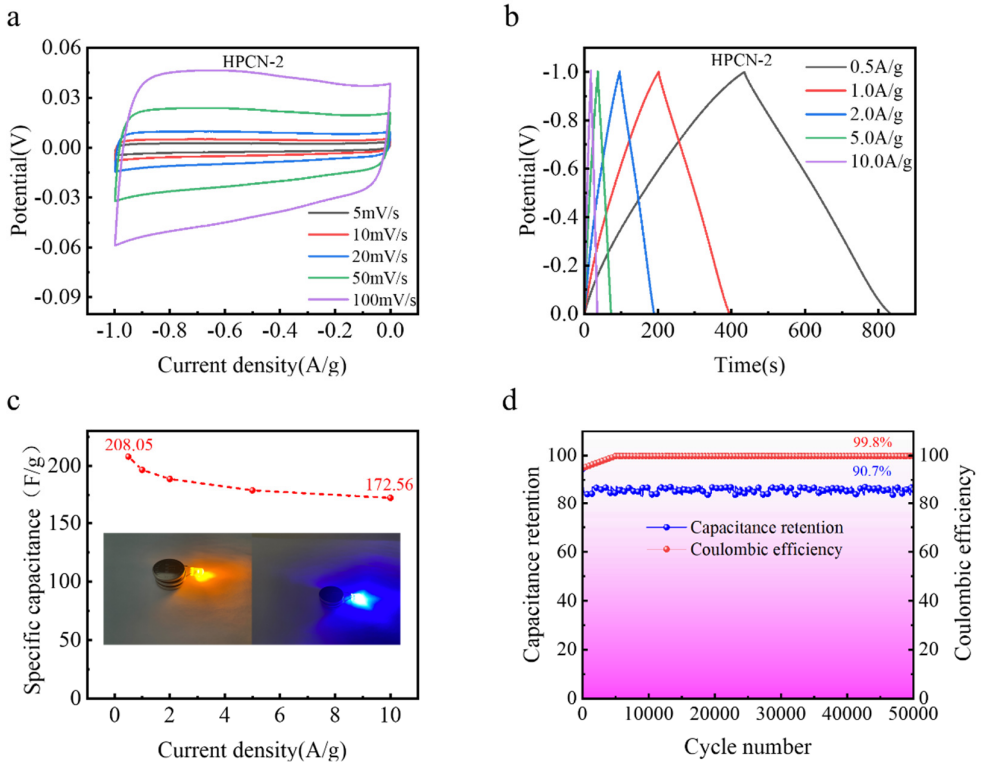

 doi:10.20944/preprints202603.2040.v1

Figure 8. (a) CV curve of HPCN-2 in symmetrical double-electrode system. (b) GCD curve of HPCN-2 in symmetrical double-electrode system. (c) Rate capability performance for HPCN-2. (d) Cycling stability diagram of HPCN-2 based symmetric supercapacitor.

4. Conclusions

This study successfully developed a nitrogen-doped porous activated carbon (HPCN-2) through a two-step process，urea-assisted hydrothermal doping of enzymatically treated lignin followed by KOH chemical activation at high temperatures. By systematically varying the urea-to-lignin mass ratio (1:1–1:4), HPCN-2 was optimized to achieve a BET surface area of 2569 m^2 g^{-1} , which synergistically enhanced pseudocapacitive behavior and interfacial charge transfer. The hierarchical pore structure (82.43% micropores) enabled rapid ion diffusion, delivering a specific capacitance of 221 F/g at 0.5 A/g in a three-electrode system. Remarkably, HPCN-2 maintained 84.4% capacitance retention (180 F/g) at 20 A/g and exhibited 90.7% capacitance retention after 50,000 cycles at 5 A/g, attributed to its robust carbon framework and minimized interfacial resistance. The exceptional performance stems from nitrogen doping (pyridinic, pyrrolic, and graphitic nitrogen species) introduced during hydrothermal synthesis, which introduces additional redox-active sites and optimizes surface chemistry. This work demonstrates that enzymatically treated lignin-derived carbons, modified via urea-KOH co-treatment, hold significant promise as advanced electrode materials for high-performance supercapacitors. The strategy provides a sustainable and scalable pathway for converting lignin biomass into high-value energy storage materials, aligning with circular economy principles and addressing critical challenges in biomass valorization.

References

1. Tong Y, Yang J, Li J, et al. Lignin-derived electrode materials for supercapacitor applications: progress and perspectives[J]. Journal of Materials Chemistry A, 2023, 11(3): 1061-1082.
2. Li W, Zhang W, Xu Y, et al. Heteroatom-doped lignin derived carbon materials with improved electrochemical performance for advanced supercapacitors[J]. Chemical Engineering Journal, 2024, 497: 154829.
3. Zhang W, Yin J, Wang C, et al. Lignin derived porous carbons: synthesis methods and supercapacitor applications[J]. Small Methods, 2021, 5(11): 2100896.
4. Rajasekaran S J, Grace A N, Jacob G, et al. Investigation of different aqueous electrolytes for biomass-derived activated carbon-based supercapacitors[J]. Catalysts, 2023, 13(2): 286.
5. Yi M, Budarin V, Yue H, et al. Lignin-derived porous carbons via nitrogen-enhanced activation for efficient supercapacitors[J]. Journal of Colloid and Interface Science, 2025: 138456.
6. Khalid M, De B S, Singh A, et al. Dual action of lignin: electrode and electrolyte for sustainable supercapacitor application[J]. ACS Applied Energy Materials, 2023, 6(15): 7857-7864.
7. Nargotra P, Sharma V, Wang H M D, et al. Biocatalysis for lignin conversion and valorization: driving sustainability in the circular economy[J]. Catalysts, 2025, 15(1): 91.
8. Zhao X, Gao P, Shen B, et al. Recent advances in lignin-derived mesoporous carbon based-on template methods[J]. Renewable and Sustainable Energy Reviews, 2023, 188: 113808.
9. Kolavada H, Gajjar P N, Gupta S K. Unraveling quantum capacitance in supercapacitors: Energy storage applications[J]. Journal of Energy Storage, 2024, 81: 110354.
10. Banerjee S, Mordina B, Sinha P, et al. Recent advancement of supercapacitors: A current era of supercapacitor devices through the development of electrical double layer, pseudo and their hybrid supercapacitor electrodes[J]. Journal of Energy Storage, 2025, 108: 115075.
11. Wu X, Liu R, Zhao J, et al. Advanced carbon materials with different spatial dimensions for supercapacitors[J]. Nano Materials Science, 2021, 3(3): 241-267.
12. Liu H, Xu T, Cai C, et al. Multifunctional superelastic, superhydrophilic, and ultralight nanocellulose-based composite carbon aerogels for compressive supercapacitor and strain sensor[J]. Advanced Functional Materials, 2022, 32(26): 2113082.

 doi:10.20944/preprints202603.2040.v1

13. Kesavan K S, Surya K, Michael M S. High powered hybrid supercapacitor with microporous activated carbon[J]. Solid State Ionics, 2018, 321: 15-22.
14. Liu W, Liu K, Du H, et al. Cellulose nanopaper: fabrication, functionalization, and applications[J]. Nano-Micro Letters, 2022, 14(1): 104.
15. Zhong M, Zhang M, Li X. Carbon nanomaterials and their composites for supercapacitors[J]. Carbon Energy, 2022, 4(5): 950-985.
16. Jiang C, Gao M, Zhang S, et al. Chitosan/graphene oxide hybrid hydrogel electrode with porous network boosting ultrahigh energy density flexible supercapacitor[J]. International Journal of Biological Macromolecules, 2023, 225: 1437-1448.
17. Zhong W, Su W, Li P, et al. Preparation and research progress of lignin-based supercapacitor electrode materials[J]. International Journal of Biological Macromolecules, 2024, 259: 128942.
18. Hao R, Wu Y, JIANG N. Recent progress on the use of lignin-based porous carbon in supercapacitors[J]. New Carbon Materials, 2025, 40(1): 50-80.
19. Li L, Wang J, Chen Z, et al. Preparation of sodium lignosulfonate-based porous carbon for supercapacitors with outstanding rate capacity and high voltage[J]. Chemical Engineering Journal, 2025, 507: 160760.
20. Zhang X, Liu S, Zhao Y, et al. Honeycomb-like hierarchical porous carbon from lignosulphonate by enzymatic hydrolysis and alkali activation for high-performance supercapacitors[J]. Energies, 2023, 16(9): 3824.
21. Feng P, Wang H, Huang P, et al. Nitrogen-doped lignin-derived porous carbons for supercapacitors: Effect of nanoporous structure[J]. Chemical Engineering Journal, 2023, 471: 144817.
22. Tian J, Liu C, Lin C, et al. Constructed nitrogen and sulfur codoped multilevel porous carbon from lignin for high-performance supercapacitors[J]. Journal of Alloys and Compounds, 2019, 789: 435-442.
23. Liu F, He J, Liu X, et al. MoC nanoclusters anchored Ni@ N-doped carbon nanotubes coated on carbon fiber as three-dimensional and multifunctional electrodes for flexible supercapacitor and self-heating device[J]. Carbon Energy, 2021, 3(1): 129-141.
24. Du L, Quan B, Xu Z, et al. Biomass-derived laser-induced graphene doped with nitrogen and sulfur for enhanced supercapacitor performance[J]. Carbon, 2025, 238: 120225.
25. Wang S, Feng J, Pan H. Facile preparation of nitrogen-doped hierarchical porous carbon derived from lignin with KCl for supercapacitors[J]. Colloids and Surfaces A: Physicochemical and Engineering Aspects, 2022, 651: 129622.
26. Sun H, Rong Y, Li J, et al. Constructing hierarchical nanosheet frameworks of nitrogen-doped carbon for enhanced energy storage performance of supercapacitors[J]. Applied Surface Science, 2025: 165041.
27. Jiang Q, Cai Y, Sang X, et al. Nitrogen-doped carbon materials as supercapacitor electrodes: a mini review[J]. Energy & Fuels, 2024, 38(12): 10542-10559.
28. Ma X, Deng J, Zhang R, et al. Hierarchical porous carbon nanoarchitectonics with honeycomb-like and N, P co-doped features for flexible symmetric supercapacitors and high-efficiency dye removal[J]. Journal of Energy Storage, 2023, 65: 107272.
29. Ran F, Yang X, Xu X, et al. Green activation of sustainable resources to synthesize nitrogen-doped oxygen-riched porous carbon nanosheets towards high-performance supercapacitor[J]. Chemical Engineering Journal, 2021, 412: 128673.
30. Liu A, Yan L, Zhang Y, et al. Nitrogen-doped coal-based microporous carbon material co-activated by HCOOK and urea for high performance supercapacitors[J]. Surfaces and Interfaces, 2024, 44: 103754.
31. Tian X L, Yu J H, Qiu L, et al. Structural changes and electrochemical properties of mesoporous activated carbon derived from Eucommia ulmoides wood tar by KOH activation for supercapacitor applications[J]. Industrial Crops and Products, 2023, 197: 116628.
32. Feng S, Fan Q, Ouyang Q, et al. Morphology and structure control of lignin-derived hierarchical porous carbon for high-performance supercapacitors[J]. Colloids and Surfaces A: Physicochemical and Engineering Aspects, 2024, 685: 133292.
33. Rustamaji H, Prakoso T, Devianto H, et al. Urea nitrogenated mesoporous activated carbon derived from oil palm empty fruit bunch for high-performance supercapacitor[J]. Journal of Energy Storage, 2022, 52: 104724.

 doi:10.20944/preprints202603.2040.v1

34. Wang T, Guo J, Guo Y, et al. Nitrogen-doped carbon derived from deep eutectic solvent as a high-performance supercapacitor[J]. ACS Applied Energy Materials, 2021, 4(3): 2190-2200.
35. Li P, Yang C, Yi D, et al. Preparation of spherical porous carbon from lignin-derived phenolic resin and its application in supercapacitor electrodes[J]. International Journal of Biological Macromolecules, 2023, 252: 126271.
36. Liu G, Chen X, Ahmed S F, et al. Urea assisted melamine N/O co-doping Activated carbon for high performance energy storage materials[J]. Journal of Power Sources, 2025, 640: 236652.
37. Zhang D, He Q, Wang D, et al. Preparation of nitrogen-doped lignin-based porous carbon materials and their application in a supercapacitor[J]. Journal of Materials Science, 2024, 59(40): 19161-19174.
38. Chen J, Lin Y, Liu J, et al. Outstanding supercapacitor performance of nitrogen-doped activated carbon derived from shaddock peel[J]. Journal of Energy Storage, 2021, 39: 102640.
39. Cao L, Li H, Xu Z, et al. Comparison of the heteroatoms-doped biomass-derived carbon prepared by one-step nitrogen-containing activator for high performance supercapacitor[J]. Diamond and Related Materials, 2021, 114: 108316.
40. Liu X, Sun B, Lin L, et al. Urea-Tris doped 3D graphene for high-stability supercapacitors[J]. Electrochemistry Communications, 2025: 108004.
41. Yin L, Hu P, Liang C, et al. Construction of self-supporting ultra-micropores lignin-based carbon nanofibers with high areal desalination capacity[J]. International Journal of Biological Macromolecules, 2023, 225: 1415-1425.
42. Khamnantha P, Homla-or C, Suttisintong K, et al. Stable lignin-rich nanofibers for binder-free carbon electrodes in supercapacitors[J]. ACS Applied Nano Materials, 2021, 4(12): 13099-13111.
43. Wang B, Xu J, Lu F, et al. Efficient utilization of lignin heterogeneity: Employing a simple approach to modulate the structure-effect relationship of lignin microspheres for its high-quality applications in supercapacitors[J]. Industrial Crops and Products, 2024, 221: 119360.
44. Li W, Wang G, Sui W, et al. Facile and scalable preparation of cage-like mesoporous carbon from lignin-based phenolic resin and its application in supercapacitor electrodes[J]. Carbon, 2022, 196: 819-827.
45. Li W, Li C, Xu Y, et al. Heteroatom-doped and graphitization-enhanced lignin-derived hierarchically porous carbon via facile assembly of lignin-Fe coordination for high-voltage symmetric supercapacitors[J]. Journal of Colloid and Interface Science, 2024, 659: 374-384.
46. Wang L, Feng X, Li X, et al. Hydrothermal, KOH-assisted synthesis of lignin-derived porous carbon for supercapacitors: value-added of lignin and constructing texture properties/specific capacitance relationships[J]. Journal of Materials Research and Technology, 2022, 16: 570-580.
47. Srinivasan S B, Devendiran S, Savunthari K V, et al. Insights into multifarious heteroatom-doped/enriched carbon-based materials and their composites: Synthesis and Supercapacitor applications– A crucial review[J]. Progress in Materials Science, 2025, 153: 101470.
48. Cai X, Zhang K, Chen W, et al. Deciphering the capacitive behavior of heteroatom-doped carbon materials with small mesopores[J]. Energy Storage Materials, 2025: 104584.
49. Lei T, Wang Y, Wang H, et al. Sustainable self-doping engineering: Transforming pulping black liquor into hierarchical sulfur-doped porous carbon architectures for advanced supercapacitor electrodes[J]. Journal of Electroanalytical Chemistry, 2025: 119448.
50. Lei T, Gai X, Wang H, et al. Petaloid-shaped hierarchical porous carbon sub-microspheres derived from lignin for high-performance supercapacitor electrodes[J]. Journal of Power Sources, 2025, 658: 238304.